Influence of Colloidal Additivation with Surfactant-Free Laser-Generated Metal Nanoparticles on the Microstructure of Suction-Cast Nd–Fe–B Alloy

Jianing Liu, Ying Yang, Franziska Staab, Carlos Doñate-Buendia, René Streubel, Bilal Gökce, Fernando Maccari, Philipp Gabriel, Benjamin Zingsem, Detlef Spoddig, Karsten Durst, Michael Farle, Oliver Gutfleisch, Stephan Barcikowski,* Konstantin Skokov, and Anna R. Ziefuß

Development of new powder feedstocks using nanoparticles (NPs) has the potential to influence the microstructure of as-built parts and overcome the limitations of current powder-based additive manufacturing (AM) techniques. The focus of this study is to investigate the impact of NP-modified magnetic microparticle powder feedstock on the microstructure of suction-cast Nd–Fe–B-based alloys. This particular casting method has been recognized for its ability to replicate, to some extent, the melting and rapid solidification stages inherent to metal powder-based AM techniques such as powder bed fusion using a laser beam. Two types of NP materials, Ag and ZrB$_2$, are used, and their effects on the grain size distribution and dendritic structures are evaluated after suction casting. Ag NPs result in smaller, more uniform grain sizes. ZrB$_2$ NPs result in uniformly distributed grain sizes at much lower mass loadings. The results show that feedstock powder surface modification with low-melting-point metal NPs can improve permanent magnets' microstructure and magnetic properties, at below 1 vol%, equal to submonolayer surface loads. Herein, the potential of using NPs to develop new powder feedstocks for AM is highlighted, significantly improving the final part's properties.

1. Introduction

Laser-based methods in additive manufacturing (AM) offer flexibility in shape design, reduced material loss, and the possibility of industrial-scale parts production.[1–3] Although laser systems in AM are becoming increasingly reliable and versatile in terms of wavelength and repetition rate, the precursor materials available for printing are often inadequate for the processing tasks currently required.[4] In powder bed fusion using a laser beam of metals (PBF-LB/M), the material choice is limited due to complex melting and solidification processes during printing, which can lead to process instability, porosity, cracking, and other defects in the as-built parts.[5,6] Therefore, the materials need to be adapted to this promising production process, which is especially relevant when functional materials like permanent magnets are being additively manufactured, where grain size and grain boundaries' nature are key to maximizing their performance. Due to its high flexibility and precision, AM might play a crucial role in future production where complex and near-net-shape structures are an important requirement.

PBF-LB/M is one of the most prominent metal AM techniques. Here, a laser beam completely melts the metal microparticle (MP) feedstocks to obtain fully dense parts after solidification.[7,8] However, extremely high solidification rates in the range of 10^3–10^5 K s^{-1}[9] of the molten metal powder

J. Liu, F. Maccari, O. Gutfleisch, K. Skokov
Functional Materials
Institute of Material Science
Technical University of Darmstadt
64287 Darmstadt, Germany

The ORCID identification number(s) for the author(s) of this article can be found under https://doi.org/10.1002/adem.202301054.

Y. Yang, C. Doñate-Buendia, R. Streubel, B. Gökce, P. Gabriel, S. Barcikowski, A. R. Ziefuß
Technical Chemistry and Center for Nanointegration Duisburg-Essen (CENIDE)
University of Duisburg-Essen
45141 Essen, Germany
E-mail: stephan.barcikowski@uni-due.de

F. Staab, K. Durst
Physical Metallurgy
Institute of Material Science
Technical University of Darmstadt
64287 Darmstadt, Germany

together with temperature gradients and layer-wise temperature cycling may lead to micro-cracks, nonequilibrium microstructure with phase segregation, and columnar grain growth, affecting the material strength.[5,10] In AlSi10Mg alloys, the fast cooling rates result in an ultrafine supersaturated Si-rich network inside each grain which positively influences the corrosion behavior; however, high residual stresses and microstructural inhomogeneity negatively affect further mechanical properties like ductility and fatigue resistance.[7,11,12] Yet, compared with structural materials (e.g., 316L, AlSi10Mg, and Ti6Al4V), functional materials such as magnetic shape memory alloys (e.g., Ni–Mn–In or Co–Ni–Ga[13]), magnetocaloric materials, or rare-earth permanent magnets (e.g., Nd–Fe–B[14,15]) are rarely produced with PBF-LB/M; thus, further research is necessary to correlate the melting-induced microstructures with the functional read-out in as-built parts.[13,16,17] The desirable microstructure for high coercivity in, e.g., Nd–Fe–B alloys consists of submicrometer- or micrometer-sized $Nd_2Fe_{14}B$ grains isolated by a paramagnetic grain boundary phase.[15,18,19] Currently, the microstructure achieved by conventional manufacturing, as applied through sintered, hot-deformed, or hydrogenation disproportionation desorption and recombination (HDDR) Nd–Fe–B magnets, cannot be achieved by PBF-LB/M.[20–23] High thermal gradients during resolidification may lead to dendritic $Nd_2Fe_{14}B$ with undesired amounts of α-Fe, negatively affecting magnetic properties.[24,25] An uneven distribution of grain size also adversely affects coercivity.[25]

To overcome this drawback, we suggest a new approach, which influences the process already at the very beginning of the process chain as we modify commercially available feedstock by adding NPs on micropowder's surface. The motivation is to limit grain growth during printing and ultimately reduce and homogenize the grain sizes in the final part.[4] Recent research shows that the employment of NPs for AM powder feedstock modification can address processability limitations, lead to grain refinement, and improve the properties of as-built parts.[26–28] Nonetheless, current research on NP-based feedstock modification often focuses on nonfunctional materials, highlighting the need for comprehensive research on such materials, along the entire process chain, powder feedstock, processing, microstructure, and part properties. Here, we propose the processing technique of suction casting (SC), as an ideal test bench,[15] as it requires only a few grams of feedstocks, allowing the fast processing of materials with different feedstock modifications. It is known that SC has far higher cooling rates (up to $10^2 \, K \, s^{-1}$, depending on the apparatus parameters such as critical section thickness as well as material properties)[29] than conventional casting. In SC, the powder is melted using an electric arc and sucked into a water-cooled mold to simulate the high cooling rates during resolidification of PBF-LB/M, producing

a similar microstructure and the same existing phases of the AM parts.[15] Hence, SC is employed as a prescreening method to exclude low-performing powders from further (then kg-scale) PBF-LB/M testing series.

In this study, Ag and ZrB_2 NPs synthesized by scalable and green synthesis method of laser ablation in liquid[30–32] are used to modify a rare-earth-based feedstock material, which is based on Nd–Fe–B, a commercial gas-atomized powder (trade name: MQP-S) consisting of magnetic exchange coupled nanograins of $Nd_2Fe_{14}B$ and α-Fe phases. Studies have demonstrated that incorporating Ag into Nd-based magnets can enhance their magnetic properties after processing with conventional sintering techniques.[33] Since Ag has a lower melting point (below 1000 °C) than Nd–Fe–B (1155 °C), it can rapidly melt and fill in vacant spaces from µm-scale-size powder packed in the powder layers with the PBF-LB/M process, resulting in higher packing density. Moreover, it is known that Ag and Nd form alloys and even intermetallic phases at high temperatures; thus, high cooling rates may stabilize high-temperature phases containing Ag and Nd.[34,35] The elevated packing density and formation of Ag-containing Nd-based phases may positively influence the magnetic performance (Hypothesis 1, **Figure 1**A). ZrB_2 melts at higher temperatures (above 3000 °C) than Nd–Fe–B; hence, ZrB_2 NPs are expected to remain solid during the melting of
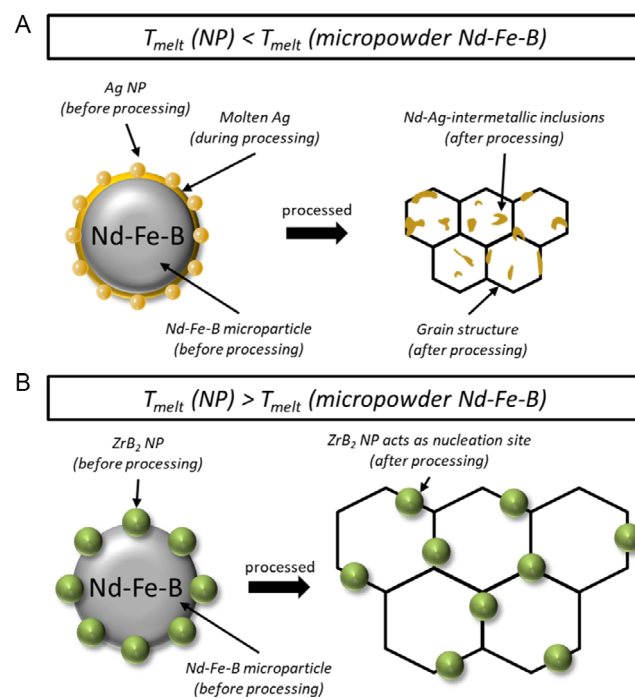
Figure 1. Schematic description of the effect of adding nanoparticles on Nd–Fe–B powder surfaces before melting-solidification processing. A) Hypothesis 1: Ag NPs additivated on the surface of Nd–Fe–B MPs will melt, forming an Ag-shell during processing and may create Nd–Ag intermetallic inclusions in the matrix during solidification, potentially assisting in decoupling the grains. B) Hypothesis 2: ZrB_2 NPs will melt later (or not at all, dependent on process parameters) and resolidify earlier than the Nd–Fe–B, which enables the nanoparticles to act as additional nucleation sites, which are starting points for grain growth, potentially leading to finer, equiaxed grains.

C. Doñate-Buendía, B. Gökce
Chair of Materials Science and Additive Manufacturing
School of Mechanical Engineering and Safety Engineering
University of Wuppertal
42119 Wuppertal, Germany

B. Zingsem, D. Spoddig, M. Farle
Faculty of Physics and Center for Nanointegration (CENIDE)
University Duisburg-Essen
47057 Duisburg, Germany

**ADVANCED
SCIENCE NEWS**

www.advancedsciencenews.com

**ADVANCED
ENGINEERING
MATERIALS**

www.aem-journal.com

Nd–Fe–B MQP-S and act as additional nucleation sites leading to finer grains during resolidification (Hypothesis 2, Figure 1B).

2. Results and Discussion

This study investigates the influence of NP loading on the suction-cast part microstructure of Nd–Fe–B-based material after melting and fast resolidification. We chose MQP-S as the "gold standard" commercially available Nd–Fe–B-type permanent magnet powder feedstock for processing,[6,36] even though strong temperature gradients are expected to reduce the magnetic properties, as it is known that the nanocomposite microstructures can be removed after AM processing.[6] It is reported by Sun et al. that powder morphology can critically influence the absorption behavior of the powder and, with this, the printing process and characteristics of the built parts.[37] The powder morphology and the magnetic properties of suction casted samples were characterized (as shown in **Figure 2**B, S1, S2, Supporting Information and Figure 6).

2.1. Feedstock Modification via Nanoparticle Additivation on the Feedstock Microparticle Surface

NPs were produced via laser ablation in liquids, enabling the synthesis of surfactant-free particles[30] without compromising the feedstock powder's flowability.[38] Moreover, cross-effectors such as organic residuals or colloidal stabilizers bear the risk of creating gases during melt processing. They may cause unwanted balling effects during processing, as shown for laser direct writing of stabilizer-containing Ag MP inks.[39] Detailed information on the NP production can be found in the Experimental and Methods section. The particle size in both cases shows a monomodal distribution, where the Ag NPs exhibit an average size of 8 nm, while the ZrB_2 NPs have an average size of 100 nm (Figure 2A). Note that the differences in particle size are intended to demonstrate the different natures of the targeted mechanisms. Hypothesis 1 aims to investigate the impact of

the formation of an NP "shell" (that is, an NP monolayer) delimiting the formed grains; the smaller size distribution facilitates adjusting the shell thickness (fraction of an NP monolayer of multiple layers) achievable. Figure 2B shows the geometric nominal distance between two Nd–Fe–B-based MPs dependent on the Ag NPs' mass loading. Note that NP melting and surface wetting will decrease the effective thickness of the Ag layer on the MP surface, resulting in partly lower values.

Hypothesis 2, however, accounts for larger particles to enable strong nucleation sites. Here, we also varied the ZrB_2 NPs' mass loading on the MP surface, testing the process with a different number of maximal nucleation centers. Here a mass loading of 1 wt% nominally enables the presence of almost 1 million nucleation centers for each MP (mean diameter of 43 μm). This number is far higher than the resulting possible grain number; however, nucleation center losses due to partial NP dissolution or aggregation during melt flow[40] have to be precompensated.

As the Ag NPs were produced in pure water, the surface decoration was performed by electrostatically controlled deposition.[41] By simply varying the pH value in the presence of the Ag NPs and Nd–Fe–B MPs, an electrostatically driven attraction force, which leads to the supporting of the Ag NPs on the Nd–Fe–B MPs (shown in Figure S1, Supporting Information), is generated. Note that the surface charges vary as a function of the pH value and that there is a pH range (pH 3–8) where NPs and Nd–Fe–B MPs show opposite signs of the surface charge (zeta potential is negative for Ag NPs[42] and positive for Nd–Fe–B MPs[43]). However, Nd–Fe–B tends to oxidize at low pHs,[44] so we carefully adjusted the pH value in the 7–8 range. While lower mass loadings of Ag NPs are homogeneously distributed, larger amounts tend to form islands on the MP surface due to agglomeration of the several NP layers deposited (see inset, Figure 2B, Figure S1, and S2, Supporting Information). To control the agglomeration, we calculated, based on a simplified geometric model,[45] the coverage of the Nd–Fe–B MPs as a function of the Ag NPs loading. It has been found that supporting 1 wt% (equivalent to 0.7 vol%) of Ag NPs on
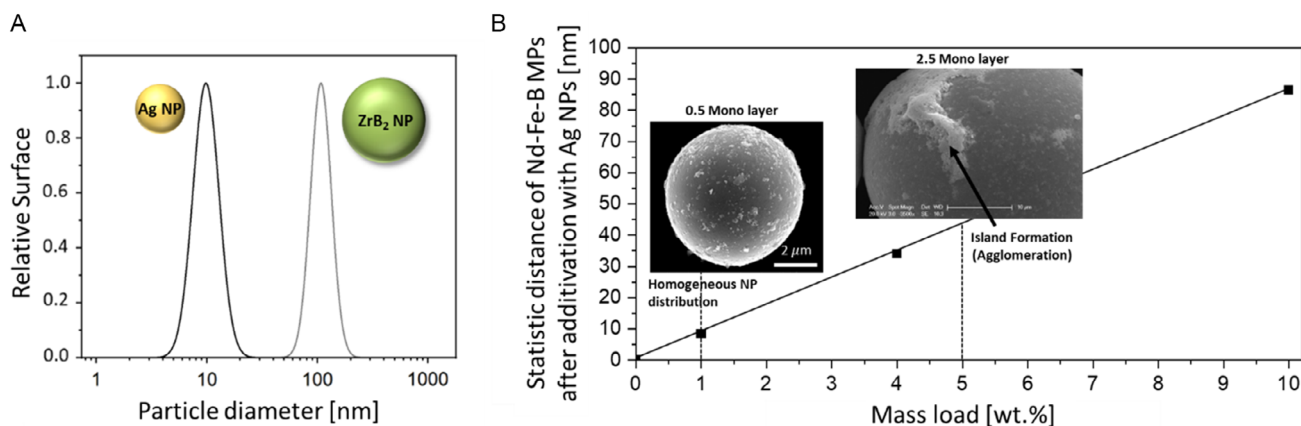
Figure 2. A) Nanoparticle size distribution after laser-based production of Ag NPs (black) and ZrB_2 NPs (gray) curves. B) Calculated statistical distance of MQP-S magnet micro-powder in dependence on the mass load of Ag NPs. The calculation assumed sphericity for both NPs and MPs and was done using a mean NP size of 8 nm and a mean MPs size of 43 nm (size distribution of the MQP-S magnet micro-powder can be found in the Supporting Information).

ADVANCED
SCIENCE NEWS

www.advancedsciencenews.com

ADVANCED
ENGINEERING
MATERIALS

www.aem-journal.com

the surface of MQP-S results statistically in a half monolayer of Ag NPs (Figure 2B), thus enabling a statistical distance between two neighboring MPs in the range of the NPs' diameter. The ZrB_2 NPs were produced in ethanol to minimize oxidation. Here, we evaporated the liquid in the presence of the feedstock, increasing the concentration of both agents in time and promoting adsorption processes by diffusion-controlled deposition.

2.2. Powder Processing and Characterization of Final Parts

After successfully modifying the feedstock powder, we processed seven Ag NP-modified feedstocks (0.1, 0.5, 0.7, 1, 4, 7, 10 wt%) loading) and four ZrB_2-NP-modified feedstocks (0.1, 0.7, 1, 2 wt% loading) via suction casting.[15,19] The NPs are intended to modify the as-built parts' microstructure, which we characterized using electron backscatter diffraction (EBSD), scanning electron microscopy (SEM)-BSE, and SEM-energy-dispersive X-Ray detector (EDX). Note that we performed heat-treatment cycles before further analysis, as required by the Nd–Fe–B permanent magnets to develop the desired magnetic properties.[19,46]

Exemplary EBSD images of as-built parts, produced via SC, for pure Nd–Fe–B-based feedstock (MQP-S) and MQP-S additivated with Ag (0.1, 1, and 7 wt%) or ZrB_2 (0.1, and 1 wt %) NPs, are shown in **Figure 3** with the indexing rate shown in Table S1 (Supporting Information). As expected, the microstructure of pure MQP-S suffers significantly from the production conditions (high-temperature gradients and fast cooling rates), resulting in an inhomogeneous grain size distribution (spots 1 and 2 in Figure 3A) containing grains with sizes far larger than 10 μm. The same applies to samples containing 0.1 and 1 wt% of Ag (Figure 3B,C). However, both spots show significantly smaller grains than the unmodified as-built part as expected from Koh et al.,[28] which have already shown the positive influence of silica-NP-additivation on the microstructure of metal matrix nanocomposites (MMNCs) after PBF-LB/M. The sample containing 7 wt% of Ag NPs (Figure 3D) and the samples decorated with ZrB_2 NPs (Figure 3E,F) revealed a more homogeneous microstructure. In all cases, the grains show dendritic growth, making it difficult to extract grain size distributions.

In summary, the EBSD results demonstrate a significant impact of NP additivation on the microstructure, which varies for the two NP materials and is affected by the NPs' loading
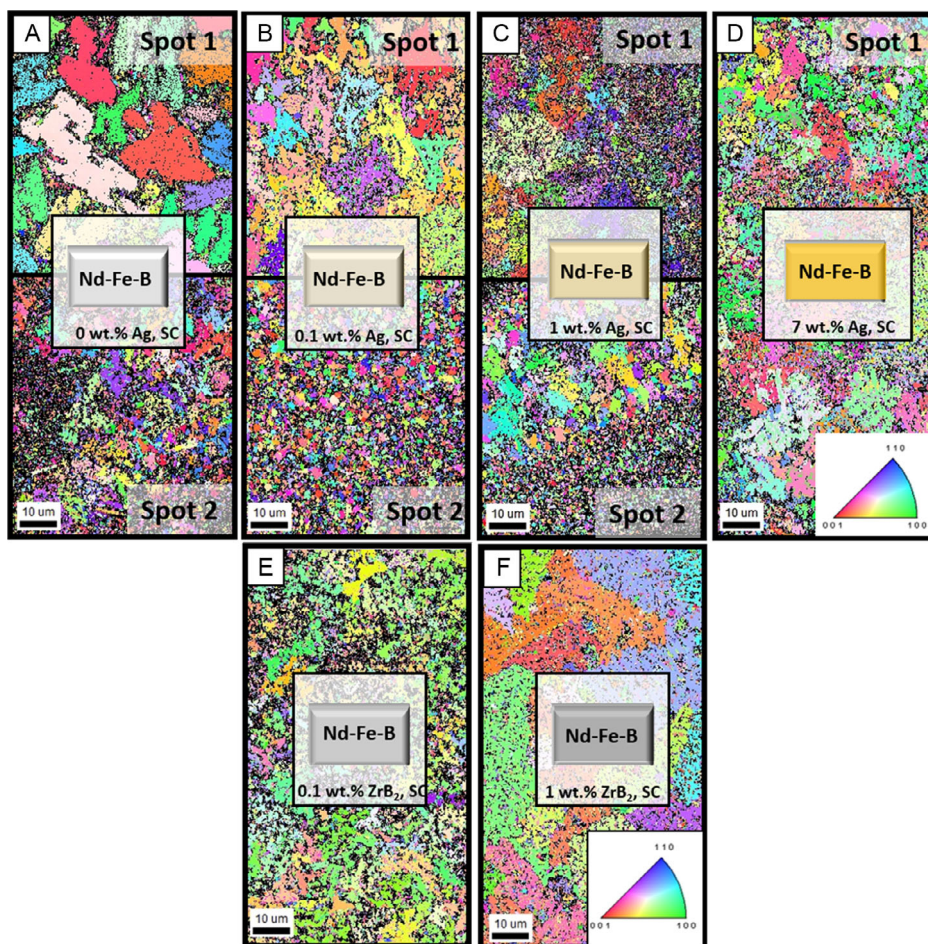
Figure 3. EBSD images of annealed SC samples from A) nonmodified B–F) and NP-additivated MQP-S powders. The indexing rate for all EBSD measurements is given in Table S1 (Supporting Information). Please note that the indexing is lower than typically expected, which we refer to the overall small grain sizes.

on the MPs. Raising the Ag NP loading leads to more uniform grain sizes but at the expense of very small grain sizes. Note that the 7 wt% sample possesses an inhomogeneous NP distribution on the feedstock powder (agglomeration/island formation) before SC, for which we cannot exclude any effect of the varied surface dispersion quality on the microstructure of the as-built part,[38] which would be interesting to reveal in future studies. Conversely, increasing the ZrB_2 loading to the same mass leads to generally good uniformity of grain sizes, with increased size observed at an increased NP mass load.

It is known that there is a correlation between grain size and the magnetic properties of permanent magnets, which allow using the magnetic properties as an additional probe to monitor changes in the latter.[19] Generally, grain sizes closer to single domain size (200–300 nm for $Nd_2Fe_{14}B$) lead to a maximized coercivity.[19] However, there is a trade-off between grain size and other mechanical properties of the material, such as strength and toughness. Therefore, finding the optimal grain size for a given application requires careful balance of magnetic and mechanical properties, which is beyond the scope of the study.
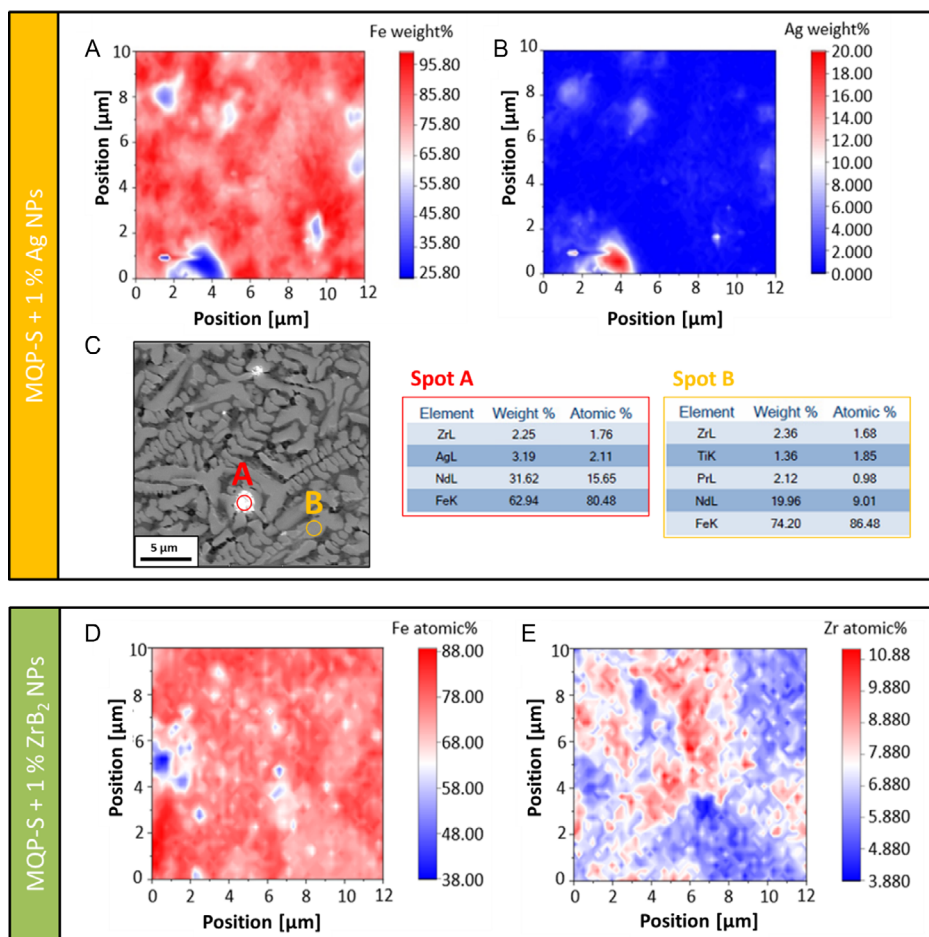
Thus, we performed SEM-BSE to explore how different types of NPs affect grain size. **Figure 4** shows that, instead of small grains separated by a nonmagnetic grain boundary phase, as proposed in Hypothesis 1, a dendritic structure forms in the samples. As shown in Figure 4A,B, the microstructure from the PBF-LB/M as-printed sample and that from as-suction cast sample are similar and comparable, confirming that SC can work as a test bench for PBF-LB/M. It has to be noted that the grain size from PBF-LB/M is dependent on the processing parameters and that from SC sample differs from area to area. As shown in Figure 4C, since the chemical composition of the samples is rich in Fe and lean in rare earth, the microstructure of suction casted and subsequently annealed sample is dendritic $Nd_2Fe_{14}B$ surrounded by α-Fe.[41] The nanocrystalline structure from the raw powder was destroyed during the remelting in the SC process, and the microstructure was much coarser afterward.[47] Figure 4D reveals the dendritic structure for one selected Ag NP-additivated as-built part. The dendritic structure is much finer and more homogeneous, which can also be observed for the ZrB_2 NP-modified as-built parts, as shown in Figure 4E–G. Here, we resolved the dendritic structure for parts with increasing ZrB_2 amount and found the increasing density of dendritic arms with increasing NP content.

SEM-EDX mapping was performed to visualize the distribution of elements in the suction-casted parts (**Figure 5**). The focus was primarily on the samples containing 1 wt% Ag NPs or ZrB_2 NPs, respectively. Despite the homogeneous Ag NPs distribution resulting after feedstock modification (Figure 2B), Ag was less uniformly distributed in the as-built part, with silver agglomeration resulting in Ag-enriched regions, showing an Ag content of more than 20 wt% higher than initially implemented, suggesting the presence of unmolten powder residues, as shown in Figure 5A,B. However, the molten areas contained hardly any Ag or had amounts below the EDX's resolution limit. To link the chemical composition from EDX mapping with the dendritic microstructure, Figure 5C shows the point analysis on a BSE image. It could be seen that the Ag is concentrated in the white spot in the interdendritic area. It has to be noted that the point is below the resolution limit, so that the exact chemical composition could only be considered as a reference, the difference between Spot A and Spot B on Ag offers a clue for the location of Ag.
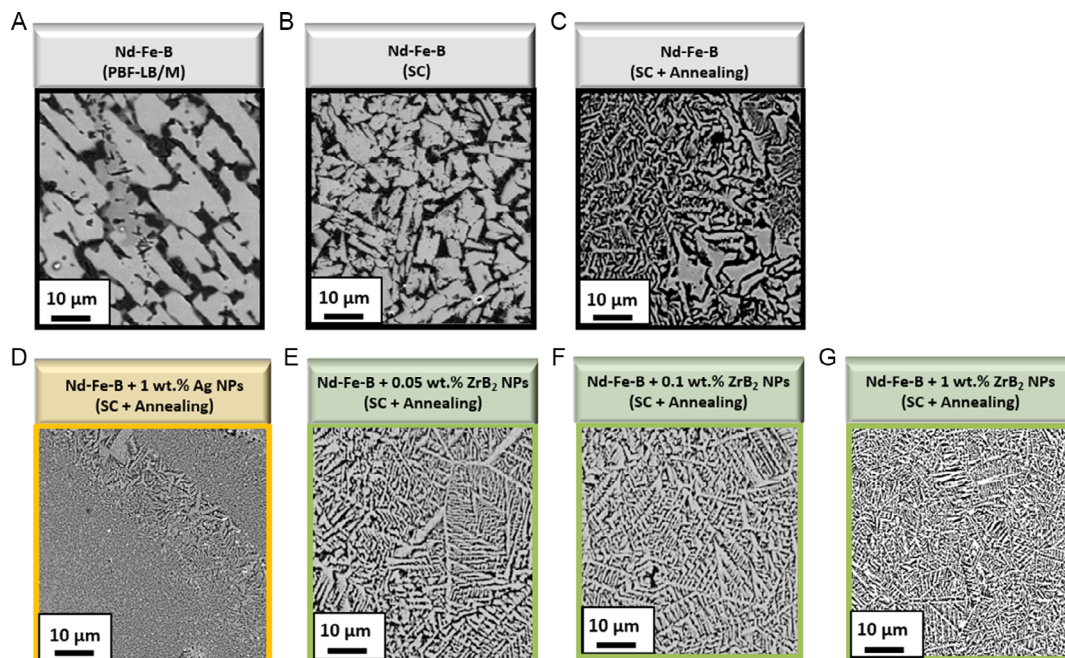
Figure 4. SEM-BSE images of A) PBF-LB/M sample (produced at 200 W laser power and 500 mm s^{-1} scanning speed), B) as-suction cast sample from unmodified MQP-S feedstock, C) annealed suction cast sample from unmodified MQP-S feedstock, D) annealed suction cast sample from modified feedstock with 1 wt% Ag NPs, E) annealed suction cast sample from modified feedstock with 0.05 wt% ZrB_2 NPs, F) annealed suction cast sample from modified feedstock with 0.1 wt% ZrB_2 NPs, and G) annealed suction cast sample from modified feedstock with 1 wt% ZrB_2 NPs.

ADVANCED
SCIENCE NEWS

www.advancedsciencenews.com

ADVANCED
ENGINEERING
MATERIALS

www.aem-journal.com

Figure 5. EDX analysis of annealed suction-cast samples. A,B) The EDX mapping. C) The EDX point analysis on a BSE-SEM image of the elements Fe and Ag in the sample suction cast from Ag NP-decorated MQP-S powder. D,E) Mapping of elements Fe and Zr in the sample cast from ZrB_2 NP-decorated MQP-S powder.

Interestingly, areas with Ag had a significantly reduced percentage of Fe. Although it is unlikely for Ag to enter the $Nd_2Fe_{14}B$ matrix, it could potentially form intermetallic phases with Nd (not detected by EDX),[33] which our study neither confirms nor negates. In comparison, Zr is wide and more evenly distributed in the cross sections. As shown in Figure 5D,E, no islands are observed due to the light color intensity (compared with Ag). We cannot exclude that it stabilizes the Nd_2Fe_{17} phase simultaneously, reducing the magnetic properties. It has to be noted that, since element B could not be precisely detected from EDX, only Zr is tracked. It is insufficient to confirm whether the Zr is from NP additivation or the original alloying element in the raw MQP-S powder.

Further note that this study aims to acquire knowledge relevant to microstructure control or, better, the limitation of grain growth during laser melting. Being fully aware that we are not yet at the point of making magnets, here we probe the magnetic properties after SC only to have additional insight into the influence of the NP addition and the microstructural changes on the magnetic response of the produced parts. We measured the hysteresis loops using a vibrating sample magnetometer and extracted, as shown in **Figure 6**, the coercivity and remanence

of the heat-treated suction-casted samples decorated with Ag NPs and ZrB_2 NPs in different mass loadings and compared them with the respective values of the suction-casted pure MQP-S (orange). The error bars show the standard deviation of the results between different batches. As expected from the literature,[36,45,48] the initial magnet material has lost its magnetic properties, showing a much-decreased remanence of 0.29 T and a coercivity of less than $50\,kA\,m^{-1}$ (Figure S3, Supporting Information). Although ZrB_2 shows a more homogeneous grain size distribution and dense dendritic structure, we do not observe any influence on the magnetic properties independent of the NPs mass loading. As noted, we cannot exclude that Zr stabilizes Nd_2Fe_{17}, which would be harmful to the hard magnetic properties and needs to be further investigated. However, the Ag NPs $\geq 1\,wt\%$ show a pronounced impact on the magnetic properties, with an increase in coercivity and remanence (shown in Figure S3, Supporting Information). For mass loadings exceeding 1 wt%, no statistically significant alteration has been detected. A mass loading of 1 wt% seems to be the sweet spot for maximizing hysteresis via Ag NP additivation, corresponding to a feedstock surface load of only half a monolayer (see the sketches in Figure 6).
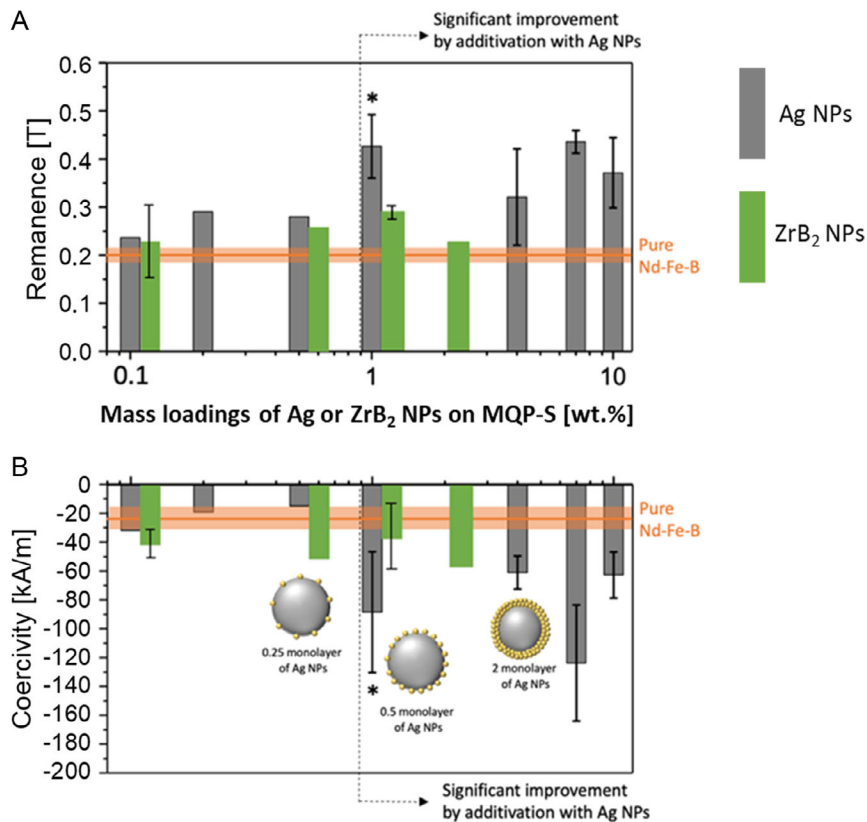
Figure 6. A) Remanence and B) coercivity of the initial Nd–Fe–B feedstock (orange horizontal line), including data after supporting 1, 4, and 10 wt% Ag NPs (gray columns), and 0.1, 0.5, 1, and 2 wt% ZrB_2 NPs (green columns) on the MP surface. Data were collected after the SC of up to three different powder batches for each loading. Error bars show the standard deviation of the results between different batches. Starting from an NP load of 1 wt% Ag, the properties (coercivity and remanence) show a significant change to those with lower Ag NPs content. We marked the significant change with a star symbol (*).

3. Conclusion

In summary, we explored how modifying magnetic feedstock powders with low vol% of nanoparticles (NPs) affect the microstructure of MQP-S after SC. Ag and ZrB_2 were used as two different types of NPs. Ag NPs were expected to melt earlier and partly dissolve in the support material during processing, resulting in a more densely packed dendritic structure and smaller and uniform grain sizes. Interestingly, this effect was observed already at low loadings of 0.7 vol% (equaling 1 wt% and is geometrically equivalent to 0.5 monolayers of Ag NPs on the magnet MP surface). In contrast, ZrB_2 resulted in uniformly distributed grain sizes at much lower mass loadings. However, no effect on magnetic properties was observed after ZrB_2 NP addition, suggesting that the NPs may be stabilizing phases harmful to the hard magnetic properties. Overall, the improved microstructure after surface additivation of 0.7 vol% (1 wt%) ligand-free Ag NPs on the magnetic micro-powders indicates that this might be a useful future strategy to be implemented into the laser powder bed fusion of Nd–Fe–B-type magnets.

4. Experimental Section

Analysis of the Magnetic Micro Powder Feedstock: This study used a gas-atomized Nd–Fe–B-based spherical powder sold by Neo Magnequench (Tuebingen, Germany). The powder was commercially known as MQP-S-11-9-20001 (referred to as MQP-S) with a declared rare-earth lean chemical composition of $Nd_{7.5}Pr_{0.7}Zr_{2.6}Ti_{2.5}Co_{2.5}Fe_{75.4}B_{8.8}$ at.% (shown in Figure S3, Supporting Information).[24,49] The average particle size was around 50 µm (shown in Figure S4, Supporting Information).[49] The powder size distribution and morphology were characterized by SEM (Philips ESEM-XL30 FEG, 20 kV) equipped with an EDX to evaluate the material composition and oxidation behavior. X-Ray fluorescence (XRF, Bruker's S8 Tiger WD-XRF) measured the initial powder composition under inert gas conditions (He atmosphere). The true density of the powder was measured using a pycnometer (Borosilicate glass 3.3. DIN ISO 3507, BRAND 25 mL type Gay-Lussac).

Preparation and Analysis of the Ag and ZrB_2 Nanoparticles: The Ag NPs were prepared by laser ablation in liquids (LAL),[30] where the pulsed laser ablated the surface of an Ag-target [20 mm (width) × 80 mm (length) × 2 mm (thickness)] immersed in water containing 0.1 µg L^{-1} NaOH. Ag NPs were prepared using a picosecond-pulsed high-power laser (500flex, Amphos GmbH,) operating at 150 W average output power. The fundamental wavelength was 1030 nm, with a laser pulse duration of 3 ps and a pulse repetition rate of 5 MHz. A galvanometer scanner (intelliSCAN-20, Scanlab AG, Purchheim, Germany) with a scanning speed of 5 m s^{-1} and an F-theta lens focusing optics $f = 254$ mm was employed. The hydrodynamic size of the synthesized Ag NPs was measured by analytical disc centrifugation (ADC, CPS instruments, INC) at a centrifugation speed of 24 000 rpm with a lower detection limit of 5 nm. The ZrB_2 NPs were produced in ethanol to minimize oxidation.

Additivation of the Nanoparticles on the Surface of the Microparticles: In a simplified picture, we added the micro powder to the produced colloid,

followed by solvent evaporation to facilitate adhesion. This confluence of actions ensured the comprehensive representation of the entire delineated process under the umbrella term "additivation". The MQP-S surface nano-additivation with Ag NPs was performed by directly mixing the powder with the colloid and post-processing to ensure the nanoparticle deposition, i.e., pH control and centrifugation.

This methodology has been previously employed for the formation of heterogeneous catalysts[50] as well as the preparation of nano-functionalized steel powders to manufacture ODS steels by AM techniques.[38] The pH of the MQP-S-Ag colloid mixture was modified to pH 7.0 followed by centrifugation at 4000 rpm and 10 °C for 15 mins. After separating the nano-functionalized MQP-S powder and the supernatant, the powder was dried in a vacuum oven at 40 °C. The ZrB$_2$ NPs were additivated by evaporation of the liquid in the presence of the feedstock, thus increasing the concentration of both agents in time and promoting adsorption processes by diffusion-controlled deposition. The morphology of the decorated micro-powders and the distribution quality of the different NP loadings had been investigated via SEM at 20 kV acceleration speed.

Preparation of the Suction Cast Bulk Samples: The prepared powder was processed by SC to emulate, with a lower powder amount, the high cooling rate and microstructure of PBF-LB/M processed samples. To prepare the powder for the SC system employed (Buehler MAM-1 arc melter), the two NP-MQP-S powder compositions were pre-pressed into a copper crucible. An electric arc then melted the material, struck under a protective Ar atmosphere, and sucked into a water-cooled mold into bulk rectangular plates with a thickness of 0.5 mm. A heat treatment was applied to increase the coercivity of the manufactured parts. First, the samples were annealed at 1000 °C for 5 h with subsequent cooling in air. Then, a second annealing at 500 °C for 3 h was applied, and the material was cooled in the furnace. For comparison of the impact of the annealing step, SEM analysis had been conducted on the resulting microstructures of samples before and after annealing.

Preparation of the PBF-LB/M Bulk Samples: Samples of unmodified MQP-S powder had been produced via PBF-LB/M to confirm the possibility of SC to replicate the achieved microstructure. The samples had been produced on a 3DSystems 350 flex under Ar atmosphere. The process parameters had been 200 W laser power, 500 mm s^{-1} scanning speed, 0.15 mm hatch distance, and 0.03 mm layer thickness.

Analysis of the Magnetic Properties of Bulk Samples: To determine the magnetic performance of the developed magnets, isothermal magnetization measurements were performed using a physical property measurement system (PPMS-VSM, Quantum Design PPMS-14) at room temperature under an applied magnetic field of up to 3 T.

Microstructural Analysis: To obtain grain orientation data, EBSD analyses were performed using a FEG-SEM (Tescan Mira3), operating at 30 kV with a step size of 0.1 μm. For each sample, three maps with an area of 60 μm × 140 μm were analyzed. A neighbor pattern averaging and re-indexing (NPAR®) post-processing routine was applied to improve the indexing rate using OIM Analysis 8.6 (EDAX) software. The same system had been applied to investigate the microstructure via SEM with a built-in EDX, operated at 20 kV acceleration speed.

Supporting Information

Supporting Information is available from the Wiley Online Library or from the author.

Acknowledgements

Conflict of Interest

The authors declare no conflict of interest.

Data Availability Statement

The data that support the findings of this study are available from the corresponding author upon reasonable request.

Keywords

[1] Y. Kok, X. P. Tan, P. Wang, M. L. S. Nai, N. H. Loh, E. Liu, S. B. Tor, *Mater. Des.* **2018**, *139*, 565.

[2] R. Shanthar, K. Chen, C. Abeykoon, *Adv. Eng. Mater.* **2023**, 2300375, https://doi.org/10.1002/adem.202300375.

[3] T. T. DebRoy, H. L. Wei, J. S. Zuback, T. Mukherjee, J. W. Elmer, J. O. Milewski, A. M. Beese, A. Wilson-Heid, A. De, W. Zhang, *Prog. Mater. Sci.* **2018**, *92*, 112.

[4] C. Doñate-Buendía, D. Gu, M. Schmidt, S. Barcikowski, A. M. Korsunsky, B. Gökce, *Mater. Des.* **2021**, *204*, 109653.

[5] F. H. Kim, S. P. Moylan, *Literature Review of Metal Additive Manufacturing Defects*; NIST AMS 100-16, National Institute of Standards and Technology, Gaithersburg, MD, **2018**, p. NIST AMS 100-16, https://doi.org/10.6028/NIST.AMS.100-16.

[6] J. Jaćimović, F. Binda, L. G. Herrmann, F. Greuter, J. Genta, M. Calvo, T. Tomše, R. A. Simon, *Adv. Eng. Mater.* **2017**, *19*, 1700098.

[7] F. Trevisan, F. Calignano, M. Lorusso, J. Pakkanen, A. Aversa, E. P. Ambrosio, M. Lombardi, P. Fino, D. Manfredi, *Materials* **2017**, *10*, 76.

[8] W. E. Frazier, *J. Mater. Eng. Perform.* **2014**, *23*, 1917.

[9] S. Pauly, P. Wang, U. Kühn, K. Kosiba, *Addit. Manuf.* **2018**, *22*, 753.

[10] A. S. Wu, D. W. Brown, M. Kumar, G. F. Gallegos, W. E. King, *Metall. Mater. Trans. A* **2014**, *45*, 6260.

[11] K. Kempen, L. Thijs, J. Van Humbeeck, J.-P. Kruth, *Phys. Procedia* **2012**, *39*, 439.

[12] K. Zyguła, B. Nosek, H. Pasiowiec, N. Szysiak, *Mater. Sci.* **2018**, *104*, 462.

[13] F. Scheibel, C. Lauhoff, S. Riegg, P. Krooß, E. Bruder, E. Adabifiroozjaei, L. Molina-Luna, S. Böhm, Y. I. Chumlyakov, T. Niendorf, O. Gutfleisch, *Adv. Eng. Mater.* **2022**, *24*, 2200069.

[14] O. Tosoni, E. Borges Mendonça, J. Reijonen, A. Antikainen, L. Schäfer, S. Riegg, O. Gutfleisch, *Addit. Manuf.* **2023**, *64*, 103426.

[15] L. Schäfer, K. Skokov, J. Liu, F. Maccari, T. Braun, S. Riegg, I. Radulov, J. Gassmann, H. Merschroth, J. Harbig, M. Weigold, O. Gutfleisch, *Adv. Funct. Mater.* **2021**, *31*, 2102148.

[16] V. Chaudhary, S. A. Mantri, R. V. Ramanujan, R. Banerjee, *Prog. Mater. Sci.* **2020**, *114*, 100688.

[17] V. Popov, A. Koptyug, I. Radulov, F. Maccari, G. Muller, *Procedia Manuf.* **2018**, *21*, 100.

[18] O. Gutfleisch, M. A. Willard, E. Brück, C. H. Chen, S. G. Sankar, J. P. Liu, *Adv. Mater.* **2011**, *23*, 821.

[19] J. M. D. Coey, *Magnetism and Magnetic Materials*, Paperback edition., Cambridge University Press, Cambridge, New York, Port Melbourne **2018**.

[20] K. Loewe, D. Benke, C. Kübel, T. Lienig, K. P. Skokov, O. Gutfleisch, *Acta Mater.* **2017**, *124*, 421.

[21] K. Khlopkov, O. Gutfleisch, R. Schäfer, D. Hinz, K.-H. Müller, L. Schultz, *J. Magn. Magn. Mater.* **2004**, *272–276*, E1937.

[22] A. Kirchner, W. Grünberger, O. Gutfleisch, V. Neu, K.-H. Müller, L. Schultz, *J. Phys. Appl. Phys.* **1998**, *31*, 1660.

[23] O. Gutfleisch, K. Khlopkov, A. Teresiak, K.-H. Muller, G. Drazic, C. Mishima, Y. Honkura, *IEEE Trans. Magn.* **2003**, *39*, 2926.

[24] M. Skalon, M. Görtler, B. Meier, S. Arneitz, N. Urban, S. Mitsche, C. Huber, J. Franke, C. Sommitsch, *Materials* **2020**, *13*, 139.

[25] J. Fidler, T. Schrefl, *J. Appl. Phys.* **1996**, *79*, 5029.

[26] J. H. Martin, B. D. Yahata, J. M. Hundley, J. A. Mayer, T. A. Schaedler, T. M. Pollock, *Nature* **2017**, *549*, 365.

[27] I. M. Kusoglu, P. Vieth, S. Heiland, F. Huber, A. Lüddecke, A. R. Ziefuss, A. Kwade, M. Schmidt, M. Schaper, S. Barcikowski, G. Grundmeier, *Procedia CIRP* **2022**, *111*, 10.

[28] H. K. Koh, J. G. S. Moo, S. L. Sing, W. Y. Yeong, *Materials* **2022**, *15*, 1869.

[29] T. Kozieł, K. Pajor, Ł. Gondek, *J. Mater. Res. Technol.* **2020**, *9*, 13502.

[30] D. Zhang, B. Gökce, S. Barcikowski, *Chem. Rev.* **2017**, *117*, 3990.

[31] F. Waag, R. Streubel, B. Gökce, S. Barcikowski, *Appl. Nanosci.* **2021**, *11*, 1303.

[32] E. Fazio, B. Gökce, A. De Giacomo, M. Meneghetti, G. Compagnini, M. Tommasini, F. Waag, A. Lucotti, C. G. Zanchi, P. M. Ossi, M. Dell'Aglio, L. D'Urso, M. Condorelli, V. Scardaci, F. Biscaglia, L. Litti, M. Gobbo, G. Gallo, M. Santoro, S. Trusso, F. Neri, *Nanomater. Basel Switz.* **2020**, *10*, 2317.

[33] T. S. Zhao, Y. B. Kim, W. Y. Jeung, *IEEE Trans. Magn.* **2000**, *36*, 3318.

[34] A. Leithe-Jasper, R. Skomski, Q. Qi, J. M. D. Coey, F. Weitzer, P. Rogl, *J. Phys. Condens. Matter* **1996**, *8*, 3453.

[35] H. Chen, X. Yang, L. Sun, P. Yu, X. Zhang, L. Luo, *J. Magn. Magn. Mater.* **2019**, *485*, 49.

[36] D. Goll, F. Trauter, T. Bernthaler, J. Schanz, H. Riegel, G. Schneider, *Micromachines* **2021**, *12*, 538.

[37] J. Sun, M. Guo, K. Shi, D. Gu, *Mater. Sci. Addit. Manuf.* **2022**, *1*, 11.

[38] C. Doñate-Buendia, P. Kürnsteiner, F. Stern, M. B. Wilms, R. Streubel, I. M. Kusoglu, J. Tenkamp, E. Bruder, N. Pirch, S. Barcikowski, K. Durst, J. H. Schleifenbaum, F. Walther, B. Gault, B. Gökce, *Acta Mater.* **2021**, *206*, 116566.

[39] A. Letzel, E. Maurer, M. Meixner, R. Poprawe, J. Stollenwerk, S. Hessner, K. Lehmann, B. Gökce, S. Barcikowski, *J. Laser Appl.* **2016**, *28*, 042004.

[40] Y. Yang, C. Doñate-Buendía, T. D. Oyedeji, B. Gökce, B.-X. Xu, *Materials* **2021**, *14*, 3463.

[41] R. Streubel, M. B. Wilms, C. Doñate-Buendía, A. Weisheit, S. Barcikowski, J. H. Schleifenbaum, B. Gökce, *Jpn. J. Appl. Phys.* **2018**, *57*, 040310.

[42] S. Rajendrachari, B. E. K. Swamy, S. Reddy, D. Chaira, Synthesis of Silver Nanoparticles and Their Applications, **2013**.

[43] R. Cao, L. Zhu, H. Liu, X. Yang, H. Nan, W. Li, *RSC Adv.* **2016**, *6*, 92510.

[44] M. Gergoric, Hydrometallurgical Treatment of Neodymium Magnet Waste. Dissertation, Department of Chemistry and Chemical Engineering Chalmers University of Technology Gothenburg, Sweden **2018**.

[45] T. Hupfeld, A. Sommereyns, F. Riahi, C. Doñate-Buendía, S. Gann, M. Schmidt, B. Gökce, S. Barcikowski, *Materials* **2020**, *13*, 3312.

[46] L. Schäfer, K. Skokov, F. Maccari, I. Radulov, D. Koch, A. Mazilkin, E. Adabifiroozjaei, L. Molina-Luna, O. Gutfleisch, *Adv. Funct. Mater.* **2023**, *33*, 2208821.

[47] C. Huber, H. Sepehri-Amin, M. Goertler, M. Groenefeld, I. Teliban, K. Hono, D. Suess, *Acta Mater.* **2019**, *172*, 66.

[48] F. Bittner, J. Thielsch, W.-G. Drossel, *Prog. Addit. Manuf.* **2020**, *5*, 3.

[49] Magnequench Inc., Material Data Sheet of MQP-S, **2006**.

[50] G. Marzun, J. Nakamura, X. Zhang, S. Barcikowski, P. Wagener, *Appl. Surf. Sci.* **2015**, *348*, 75.

2301054 (9 of 9)